

## Supporting information for:

# What controlled the thickness of continental crust in the Archean?

**Vuong V. Mai<sup>1</sup> and Jun Korenaga<sup>1</sup>**

<sup>1</sup>*Department of Earth and Planetary Sciences, Yale University, PO Box 208109, New Haven, Connecticut 06520-8109, USA. Email address: jun.korenaga@yale.edu*

### Contents of this file:

Reanalysis of the deformation data of quartz aggregates

Strain rate modeling

Figures S1 to S9

Tables S1 to S7

## 1 Reanalysis of the deformation data of quartz aggregates

As the rheology of quartz aggregates plays a critical role in evaluating the strength of upper continental crust, we conduct a quantitative review of major existing experimental studies, by reanalyzing original deformation data with a rigorous statistical analysis. In what follows, we describe selected deformation studies, show how data are prepared, explain our statistical approach, and provide steps in our inversion and analytical procedure. Lastly, we summarize inversion results and provide a justification for our preferred flow law for quartz aggregates.

### 1.1 Quartz rheology

Flow laws are generally described by relating the strain rate to the applied stress and other state variables such as temperature and grain size. Flow laws for dislocation creep, diffusion creep, and grain boundary sliding (GBS) may be defined, respectively, as:

$$\dot{\epsilon}_{\text{dis}} = A_1 \sigma^{n_1} \exp\left(-\frac{Q_1}{RT}\right), \quad (\text{S1})$$

$$\dot{\epsilon}_{\text{dif}} = A_2 d^{-m_3} \sigma \exp\left(-\frac{Q_2}{RT}\right), \quad (\text{S2})$$

$$\dot{\epsilon}_{\text{GBS}} = A_3 d^{-m_3} \sigma^{n_3} \exp\left(-\frac{Q_3}{RT}\right), \quad (\text{S3})$$

where  $\dot{\epsilon}$  is the strain rate ( $\text{s}^{-1}$ ),  $A$  is the pre-exponential factor ( $\text{s}^{-1} \text{MPa}^{-n} \mu\text{m}^m$ ),  $\sigma$  is the differential stress (MPa),  $n$  is the stress exponent,  $R$  is the gas constant, and  $T$  is the temperature (K). Grain size sensitivity is specified by the grain size,  $d$  ( $\mu\text{m}$ ), and the grain-size exponent,  $m$ . Temperature sensitivity is controlled by the activation energy,  $Q$  ( $\text{J mol}^{-1}$ ). In the presence of water content, we may include the water fugacity,  $f_{\text{H}_2\text{O}}$  (MPa), or water content,  $C_{\text{OH}}$  ( $\text{H}/10^6\text{Si}$ ), with their associated exponent,  $r$ .

### 1.2 Deformation Data

Data chosen for our reanalysis encompass the following ductile flow law regimes: dislocation creep (Gleason & Tullis, 1995; Rutter & Brodie, 2004a), diffusion creep (Rutter & Brodie, 2004b), and grain boundary sliding (Fukuda, Holyoke, & Kronenberg, 2018). Here we briefly summarize the experimental conditions and results from these papers.

### 1.2.1 Rutter & Brodie (2004a) [RB04a]

To better control grain size and water content, Rutter & Brodie (2004a) performed deformation experiments in the dislocation creep regime using synthetic quartzite prepared from crushed aggregates of Brazilian quartz. Hot-pressed samples were separated into grain sizes of three diameters: 0.4, 1.3, and 4.5  $\mu\text{m}$ . RB04a measured the initial water content to be  $\sim 15 \text{ H}/10^6 \text{ Si}$ . A weight loss corresponding to 1-2 molecular layers of water adsorbed during heating was determined for grain sizes of 0.4  $\mu\text{m}$ . Some 0.4  $\mu\text{m}$  samples were pre-dried at 1373 K to remove adsorbed water, while the rest were kept as-ground. Of all the grain size fractions, only the 0.4  $\mu\text{m}$  as-ground samples showed grain growth due to large amounts of adsorbed water. These samples grew to  $\sim 12 - 20 \mu\text{m}$ , which were used in RB04a to study dislocation creep. The finer grained samples were reserved for the study of diffusion creep in Rutter & Brodie (2004b)[RB04b].

RB04a reported the uncertainty for temperature as  $\pm 7 \text{ K}$ . For our inversion that will be described later, we assume an uncertainty of  $\pm 1\%$  for confining pressure,  $\pm 5\%$  for strain rate, and  $\pm 5 \text{ MPa}$  for stress. Deformation experiments were conducted in a gas apparatus in the  $\beta$ -quartz field, at a confining pressure of 300 MPa and at temperatures between 1273 - 1473 K. RB04a found dislocation creep to be the dominant deformation mechanism, with some contributions from grain boundary sliding. RB04a reported the flow law determined from their experimental results to be:

$$\dot{\epsilon} = 10^{-4.93} \sigma^{2.97} f_{\text{H}_2\text{O}} \exp(-242000/RT). \quad (\text{S4})$$

The pre-exponential factor was re-calculated from  $A = A' f_{\text{H}_2\text{O}}^r$ , where it was assumed that  $r = 1$  and  $f_{\text{H}_2\text{O}} = 300 \text{ MPa}$ .

### 1.2.2 Rutter & Brodie (2004b) [RB04b]

The starting material was the same as those discussed in the previous section. In RB04b, fine-grained samples of sizes 0.4 (pre-dried), 1.3, and 4.5  $\mu\text{m}$  were used. RB04b reported that no significant grain growth was observed for these size fractions. For our inversion, we assume an uncertainty of  $\pm 1\%$  for confining pressure,  $\pm 5\%$  for strain rate, and  $\pm 3\%$  for stress. Deformation experiments were conducted in the same  $\beta$ -quartz regime as in RB04a. At stresses  $> 200 \text{ MPa}$ , RB04b found contributions from dislocation creep. A grain-size sensitive flow law (eq. S2) was therefore determined using data with stresses below 200 MPa:

$$\dot{\epsilon} = 10^{-0.4} \sigma^{1.0} d^{-2.0} \exp(-220000/RT). \quad (\text{S5})$$

### 1.2.3 Gleason & Tullis (1995) [GT95]

Gleason & Tullis (1995) derived a grain-size insensitive flow law using a Griggs-type apparatus with a molten salt cell (MSC) to minimize strength contributions from the confining medium. They reported the strengths of quartzite samples measured in the MSC to be half of those measured in solid media. Here we use data reported for the flow law determined from melt-free samples.

Black Hills Quartzite (BHQ) was chosen as the starting material. The average starting grain size was  $\sim 100 \mu\text{m}$ , with an initial water content of the order of  $1000 \text{ H}/10^6 \text{ Si}$  ( $\sim 0.15 \text{ wt.}\% \text{ H}_2\text{O}$ ). For strain rate-stepping experiments, the range of confining pressure and temperature were 1560 - 1700 MPa and 1273 - 1373 K, respectively. Strain rates varied between  $10^{-4.1}$  and  $10^{-5.8} \text{ s}^{-1}$ . For temperature-stepping experiments, the ranges for confining pressure and strain rates were 1440 - 1580 MPa and  $10^{-4.8}$  and  $10^{-5.8} \text{ s}^{-1}$ , respectively, and the temperature was varied between 1173 - 1373 K. GT95 reported an uncertainty of  $< 3 \text{ K}$  for the temperature. For our inversion, we assumed an uncertainty of 1% for confining pressure, 5% for strain rate,  $\pm 10 \text{ MPa}$  for stress, and 10% for grain size.

In their calculation of the flow law from melt-free samples, GT95 used only data from the dislocation creep regime, and only at steady-state flow stresses. The dislocation flow law determined in GT95 is:

$$\dot{\epsilon} = 10^{-3.96} \sigma^{4.0} f_{\text{H}_2\text{O}} \exp(-223000/RT). \quad (\text{S6})$$

GT95 noted that the water-dependence of defects must be constrained in order to extrapolate results into geologic strain rates. Although GT95 did not control  $f_{\text{H}_2\text{O}}$ , they calculated a  $\log f_{\text{H}_2\text{O}}$  value of 3.71. Citing data from Kronenberg & Tullis (1984) and Gleason & Tullis (1993), GT95 suggested a water fugacity exponent of  $\sim 1.0$  under their experimental conditions.

#### 1.2.4 Luan & Paterson (1992) [LP92]

Luan & Paterson (1992) used synthetic quartz samples produced from three types of starting materials: natural quartz powder, impure silica gel, and high-purity silicic acid. However, due to lack of steady-state data on natural quartz-origin and significant contributions from grain boundary sliding in silica gel-origin samples, we consider only their flow law derived from samples of silicic acid origin. The initial grain sizes for these specimens were between 20 - 30  $\mu\text{m}$ .

LP92 reported an uncertainty of  $\pm 5\text{K}$  for the temperature and 500 H/10<sup>6</sup>Si for water content. For our inversion, we assume an uncertainty of  $\pm 1\%$  for confining pressure,  $\pm 5\%$  for strain rate,  $\pm 3\%$  for stress, and  $\pm 10\%$  for grain size. Strain rate- and temperature-stepping experiments were conducted in a gas apparatus at 300 MPa confining pressure, and all experimental runs were conducted within the  $\beta$ -quartz stability field.

Although LP92 determined the stress exponent and the activation energy, they did not report the pre-exponential factor. Lu & Jiang (2019) calculated an average for this value by substituting  $n$  and  $Q$  into the grain-size insensitive flow law (eq. S1). The flow law for silicic acid-origin specimens is then determined as:

$$\dot{\epsilon} = 10^{-7.92} \sigma^{4.0} \exp(-152000/RT). \quad (\text{S7})$$

#### 1.2.5 Fukuda et al. (2018) [F18]

Fukuda et al. (2018) conducted strain rate-, temperature-, and pressure-stepping experiments on hot-pressed, natural quartz aggregates with grain sizes of 1.7 - 12.0  $\mu\text{m}$ . To maintain fully water-saturated samples, experimental runs were conducted in a Griggs-type apparatus using NaCl as the pressure medium. To correct the flow stresses for solid salt assemblies, F18 used the stress correction suggested by Holyoke & Kronenberg (2010):

$$\sigma_{gas} = 0.7 \times \sigma_{Griggs} - 48 \text{ MPa}, \quad (\text{S8})$$

which is estimated to have an accuracy of  $\pm 30$  MPa. Experiments were conducted under temperatures between 873 and 1223 K, confining pressures between 0.9 - 1.5 GPa, and strain rates between  $10^{-3.3}$  and  $10^{-5.9} \text{ s}^{-1}$ . Here we consider only their flow law derived from data conducted under high temperatures (1073 - 1223 K), where the grain-size sensitivity of creep and fugacity exponent was determined. F18 suggested that deformation occurred by “a combination of intracrystalline and grain boundary processes,” and assumed a flow law in the form of eq. (S3).

F18 reported an uncertainty of  $\pm 1$  K for temperature and  $\pm 30$  MPa for confining pressure. We assume an uncertainty of  $\pm 5\%$  for strain rate,  $\pm 30$  MPa for stress,  $\pm 10\%$  for grain size, and  $\pm 10\%$  for water fugacity. F18 calculated the water content from IR spectra, using a calibration from Aines, Kirby, & Rossman (1984). The water content was determined to be 3500 H/10<sup>6</sup>Si on average. The water fugacities were calculated using the molar volume and equation of state for pure water from Pitzer & Sterner (1994) and Sterner & Pitzer (1994), respectively. To determine the grain size at each deformation step, F18 conducted grain

growth experiments and determined the grain growth equation (Karato, 2008) under a confining pressure of 1.5 GPa and temperatures between 1173 - 1273 K:

$$L^2 - L_0^2 = 0.97t \exp(-72000/RT), \quad (\text{S9})$$

where  $L$  and  $L_0$  are the final and initial grain size ( $\mu\text{m}$ ), respectively, and  $t$  is time (s). The initial grain size at each experimental run was calculated using hot-pressing data, assuming an initial grain size of 1.7  $\mu\text{m}$  for the starting material.

F18 resolved the stress exponent  $n$  from strain rate-stepping experiments at 1073 and 1173 K, the fugacity exponent  $r$  from pressure-stepping experiments, the activation energy  $Q$  from temperature-stepping experiments, and the grain-size exponent  $m$  from grain growth and deformation experiments. Their flow law is given as:

$$\dot{\epsilon} = 10^{-2.97} \sigma^{1.7} d^{-0.51} f_{\text{H}_2\text{O}}^{1.0} \exp(-183000/RT). \quad (\text{S10})$$

### 1.3 Data pre-processing for inversion

#### 1.3.1 Data selection

LP92's data from natural quartz-origin samples did not show steady-state behavior, and their silica gel samples showed significant contributions from grain boundary processes. In this study, we include only data from their silicic acid-origin specimens, for which both steady-state and dislocation behavior were observed. From LP92's Table 4, we ignore re-cored samples, those without pre-drying, and any experimental runs which lacked water content data. In GT95, we ignore samples deformed in the  $\alpha$ -quartz regime.

#### 1.3.2 Stress corrections

The flow stresses in GT95 were corrected to those measured in a gas apparatus following the stress calibration suggested by Holyoke & Kronenberg (2010):

$$\sigma_{\text{gas}} = 0.73 \times \sigma_{\text{GriggsMSC}}, \quad (\text{S11})$$

which is estimated to have an accuracy of  $\pm 10$  MPa.

#### 1.3.3 Estimating grain size

For experiments with incomplete grain size data, we calculate grain sizes at different temperature steps following the grain growth equation from Karato (2008):

$$L^p - L_0^p = k_0 t \exp(-Q/RT), \quad (\text{S12})$$

where  $L$  is the grain size ( $\mu\text{m}$ ) after some time  $t$  (s),  $L_0$  is the initial grain size ( $\mu\text{m}$ ),  $p$  is a constant,  $k_0$  is a constant factor,  $Q$  is the activation energy ( $\text{J mol}^{-1}$ ),  $R$  is the gas constant, and  $T$  is the absolute temperature (K).

For data from GT95, we use  $p = 2$ ,  $k_0 = 0.97$ ,  $L_0 = 100 \mu\text{m}$ , and  $Q = 72 \text{ kJ mol}^{-1}$ , calculated from data in grain growth experiments conducted under similar high-pressure conditions by Fukuda et al. (2018). The time at each step was determined by dividing the total strain at each step<sup>1</sup> by the strain rate.

Data from LP92 were all collected at a confining pressure of 300 Ma, and for temperature-stepping experiments where intermediate grain sizes were not reported, we used eq. S12 to interpolate at each deformation step, with  $L_0 = 25 \mu\text{m}$ ,  $p = 2$ ,  $k_0 = 10^2 \mu\text{m}^p \text{s}^{-1}$ , and  $Q = 80 \text{ kJ mol}^{-1}$ , based the re-calculation of data from Tullis & Yund (1982) in Karato (2008).

<sup>1</sup>Estimated from Figures 3 and 6 in Gleason & Tullis (1995).

## 1.4 Nonlinear inversion with Markov-chain Monte Carlo

Broadly speaking, Markov-chain Monte Carlo (MCMC) sampling is a way to model probability distributions, often non-linear and multi-dimensional, for which direct methods may prove either too inefficient or insufficient. MCMC gives an approximation of this distribution through repeated random sampling, which comprises the ‘Monte Carlo’ part of its namesake. The ‘Markov-chains’ describe the process by which each sample is chosen. The algorithm indeed begins with a single random sample, but every subsequent sample is chosen by an estimation of its conditional probability such that a chain can be imagined to weave through the probability distribution, exploring the most populous and significant regions of this space. We avoid completely eliminating samples which have low probabilities, as that could prevent our chains from fully exploring the space should local extremities exist.

Details on the sampling method used in this study are outlined in Korenaga & Karato (2008) and Mullet, Korenaga, & Karato (2015). Here, we provide a brief description of the main principle by which the algorithm operates:

- A misfit function measures the disparity between the observed and predicted strain rates.
- The algorithm systematically samples from a theoretically infinite model space based on the conditional likelihood, which is calculated from the misfit function.
- At each iteration, the algorithm randomly perturbs one parameter, and whether a given perturbation is adopted or not is then decided by comparing the need to minimize the misfit and the need to explore the model space.
- Given enough<sup>2</sup> iterations, the algorithm should sufficiently explore the model space such that a collection of sampled solutions can be regarded as a good approximation to the probability distribution associated with the model space.

Using this MCMC strategy, we perform simultaneous inversion of flow laws from deformation data. The ‘goodness’ of fit is measured by the  $\chi^2$  (misfit), for which the ideal value is  $\chi^2 \sim N$ , where  $N$  is the number of data, which means that data are explained by a fitted flow law within their uncertainties on average. We note that since  $\chi^2$  measures model-data misfit, a small  $\chi^2$  does not necessarily relate to a well-constrained model. It is common in our results for models to fit well with data but remain poorly constrained when extrapolating, as is often the case with diffusion creep. During our MCMC inversion, the target of minimization is the misfit function defined in Mullet et al. (2015), because it better prevents parameter bias. On the other hand, reported misfit in our results corresponds to the original misfit defined in Korenaga & Karato (2008) since it takes into account the uncertainty of all variables.

## 1.5 Inversion procedure

To assist our MCMC simulation with convergence and to constrain our models, we impose some conditions on the algorithm. Here we list our assumptions and introduce the procedure used in our inversion.

Inversions are done on composite flow laws, defined as a summation of contributions from dislocation and diffusion creep:

$$\dot{\epsilon}_{\text{comp}} = \dot{\epsilon}_{\text{dis}} + \dot{\epsilon}_{\text{dif}} \quad (\text{S13})$$

where  $\dot{\epsilon}_{\text{dis}}$  and  $\dot{\epsilon}_{\text{dif}}$  are defined by eqs. S1 and S2. For F18 data, we also invert for a GBS flow law, defined in eq. S3.

---

<sup>2</sup>‘Enough’ refers to convergence. Since there is no direct test for convergence, only for failure to converge, we use two diagnostics: the autocorrelation function and test for reproducibility, discussed in Korenaga & Karato (2008) and Mullet et al. (2015).

Each inversion resolves all the parameters for an assumed flow law. In this study, we perform  $10^6$  MCMC inversions on each data set, such that the output contains  $10^6$  flow law models. In our analysis of inversion results, we show the distribution of these models and compare the average model to those reported in each respective study.

### 1.5.1 A priori bounds

For composite inversions with no water information (RB04ab and GT95), we imposed the following a priori bounds:  $1.0 \leq m \leq 6.0$ ,  $1.0 \leq n \leq 6.0$ , and  $0 \leq Q \leq 600 \text{ kJ mol}^{-1}$ . Wet composite and GBS inversions (LP92 and F18) had additional constraints on the fugacity exponent:  $1.0 \leq r \leq 5.0$ .

### 1.5.2 Inter-run bias

The idea of modeling inter-run bias as part of inversion was introduced in Korenaga & Karato (2008) to necessarily characterize systematic differences between experiments and better quantify these uncertainties. Inter-run biases are computed between different groups of data. The meaning of these ‘groups’ depends on the context. In the inversion of RB04ab, data from RB04a and RB04b were considered separate groups. In the inversion of GT95, LP92, and F18, data from each experimental run was considered its own group. We assume that systematic bias is more or less uniform within the same group but may vary across different groups. If this assumption is correct, the inter-run bias works well at correcting for systematic bias. Thus, in RB04ab, the inter-run bias characterizes the systematic differences between dislocation-creep-dominated and diffusion-creep-dominated experiments. In GT95, LP92, and F18, the inter-run bias characterizes differences between experimental runs.

Typically, inter-run biases are small and range in the order of  $10^{-1}$  to  $10^1$ . In this document, we do not report inter-run bias except where its magnitude is noteworthy.

### 1.5.3 Re-sampling

To reduce correlation between MCMC iterations, we re-sample our results. For this study, we discard the first 1,000 iterations and re-sample the rest of iterations at an interval of 100 iterations.

## 1.6 Inversion results

Here we provide a summary of our inversion results, with a series of figures comparing deformation data with our flow-law predictions (Figures S1-S6). Also, the a posteriori probability distributions of flow-law parameters are shown for all inversions (Figure S7).

From the re-sampling of  $10^6$  MCMC iterations done on each data set, we construct  $10^3$  flow laws to show the distribution of our flow-law predictions in the strain rate-stress, strain rate-temperature, and strain rate-grain size spaces. In each respective space, all other parameters are kept constant. Data are normalized using the average flow-law parameters.

### 1.6.1 RB04ab

Data reported in Table 1 of RB04a and RB04b are combined for a simultaneous inversion of the composite flow law (eq. S13). Our flow law for dislocation creep agree well with RB04a data (Figure S1). However, the diffusion creep component of our composite inversion predicts strain rates higher than predicted by the original study by a few orders of magnitude (compare solid black and cyan lines in Figure S1). We attribute this discrepancy to the large systematic bias between RB04a and RB04b data, as the inter-run bias is significant and in the order of  $10^3$  (Figure S2). This is not expected as these experiments were conducted

in the same lab around the same time, and samples from both experiments came from the same starting materials. RB04b did not account for this bias in their calculation of the flow law, which may explain the gap between their flow law and our flow law for diffusion creep.

With an average  $\chi^2/N$  of 58, our flow laws for RB04ab data are:

$$\begin{aligned}\dot{\epsilon}_{\text{dis}} &= 10^{-5.2 \pm 1.0} \sigma^{3.5 \pm 0.3} \exp(-(208 \pm 19)/RT), \\ \dot{\epsilon}_{\text{dif}} &= 10^{1.0 \pm 1.6} d^{-2.4 \pm 0.8} \sigma \exp(-(213 \pm 42)/RT).\end{aligned}$$

### 1.6.2 GT95

Data from Tables 1 and 2 in GT95 are used for the inversion of a composite flow law. Our inversion gave poor constraints on diffusion creep (Figure S3), which we attribute to the limited range of grain size. In general, diffusion creep parameters throughout our inversions are more poorly constrained than those for dislocation creep. However, we find that it is still useful to invert for a composite flow law should deformation conditions occur near the boundary between dislocation and diffusion creep. The stress-strain rate relation shows minor contributions from diffusion creep at low stresses (Figure S3). Although poorly constrained, modeling diffusion creep is necessary to characterize this subtle shift.

With an average  $\chi^2/N$  of 0.67, our flow laws for GT95 data are:

$$\begin{aligned}\dot{\epsilon}_{\text{dis}} &= 10^{-6.7 \pm 1.4} \sigma^{3.9 \pm 0.3} \exp(-(145 \pm 31)/RT) \\ \dot{\epsilon}_{\text{dif}} &= 10^{4.8 \pm 6.3} d^{-2.7 \pm 1.8} \sigma \exp(-(182 \pm 129)/RT).\end{aligned}$$

We find that the flow law reported by GT95 predicts strain rates a few magnitudes larger than our flow law, probably because their way of estimating the pre-exponential factor  $A$  is inaccurate and subject to large uncertainties. GT95 determined the stress exponent from two strain rate-stepping experiments and the activation energy from two temperature-stepping experiments. In their calculation of the pre-exponential factor, the uncertainty in  $n$  and  $Q$  produces a wide range of values in  $A$ . For  $n$  of 4.1,  $A$  is between  $10^{-7}$  and  $10^{-3}$ ; for  $n$  of 3.9,  $A$  is between  $10^{-9}$  and  $10^{-7}$ . For a  $Q$  of 225 kJ mol $^{-1}$ ,  $A$  is between  $10^{-6}$  and  $10^{-3}$ ; for a  $Q$  of 220 kJ mol $^{-1}$ ,  $A$  is between  $10^{-6}$  and  $10^{-2}$ . GT95 reported the average of these values. However, considering the wide range of  $A$ , the arithmetic average is not very meaningful.

A common problem in the conventional analysis of rock deformation data is that each flow-law parameter is independently and sequentially determined so that the calculation of each subsequent parameter depends on the robustness of previous parameters, which are themselves often poorly constrained. With the traditional linear regression method, not only are flow-law parameters themselves difficult to be resolved, but so are their respective uncertainties. Furthermore, linear methods are unable to characterize the effects of contributions from multiple deformation mechanisms.

### 1.6.3 LP92

Using data on silicic acid-origin specimens from Table 4 of LP92, we initially invert for a composite flow law. However, our composite inversion results indicate that contributions from diffusion creep were negligible, and samples deformed primarily in the dislocation regime. Thus, we present results from inversion for only dislocation creep flow law as opposed to a composite flow law.

With an average  $\chi^2/N$  of 4.8, our dislocation creep flow law from LP92 data is:

$$\dot{\epsilon}_{\text{dis}} = 10^{-11.2 \pm 1.8} \sigma^{3.4 \pm 0.3} C_{OH}^{1.1 \pm 0.3} \exp(-(138 \pm 42)/RT).$$

Predictions from our flow law and the original LP92 flow law both explain the data well (Figure S4), though our estimate of the stress exponent ( $\sim 3.4$ ) is notably lower than their estimate (4.0).

### 1.6.4 F18

Using data from Table 3 of F18, we perform two separate inversions: one composite inversion (Figure S5) and one GBS inversion (Figure S6), to compare with the GBS flow law determined by F18 (eq. S10).

With a  $\chi^2/N$  of 10.4, our flow laws for composite rheology from F18 data are:

$$\begin{aligned}\dot{\epsilon}_{\text{dis}} &= 10^{-19.7 \pm 4.4} \sigma^{3.6 \pm 0.2} f_{\text{H}_2\text{O}}^{1.9 \pm 1.1} \exp(-(30 \pm 12)/RT), \\ \dot{\epsilon}_{\text{dif}} &= 10^{-4 \pm 0.4} d^{-1.06 \pm 0.05} f_{\text{H}_2\text{O}}^{1.04 \pm 0.08} \sigma \exp(-(120 \pm 12)/RT).\end{aligned}$$

With a  $\chi^2/N$  of 18.8, our GBS flow law is:

$$\dot{\epsilon}_{\text{GBS}} = 10^{-8.8 \pm 0.7} d^{-0.46 \pm 0.05} f_{\text{H}_2\text{O}}^{1.3 \pm 0.15} \sigma^{1.48 \pm 0.08} \exp(-(76 \pm 5)/RT).$$

Although the GBS flow law seems to be better when comparing model predictions with normalized data (Figures S5 and S6), the  $\chi^2/N$  is actually smaller for the composite flow law (10.4) than for GBS (18.8).

We observe that a major difference between our GBS flow law and F18's GBS flow laws are different values for the stress exponent  $n$ . F18 reported that "strengths of the final deformation step ... are generally lower than in deformation steps performed at similar strain rates in the initial deformation step," and that "differences are likely due to evolution of grain size." Here, we see that the traditional analytical approach of independently resolving each parameter neglects the effects of grain size during the determination of the stress exponent, which increases the error of  $n$ . F18 calculated values for  $n$  from six strain rate-stepping experiments conducted at high temperatures (1073 - 1223 K), with values ranging between 1.5 and 1.8. F18 report the average for these values to be  $1.7 \pm 0.2$ .

F18 determined the water fugacity exponent through pressure-stepping experiments at 1073 K. Relating the differential stress to water fugacity through the following relation:

$$\Delta \log \sigma = -\frac{r}{n} \Delta \log(f_{\text{H}_2\text{O}}) \quad (\text{S14})$$

and using the previously determined value of  $n$ , F18 calculated the water fugacity and its exponent  $r$ . The calculation of  $f_{\text{H}_2\text{O}}$  and  $r$  was done at a single temperature (1073 K), for which 4 data points were available. Compared to the fugacity exponent calculated by F18,  $r = 0.51$ , our value of  $r = 1.3 \pm 0.15$  agrees more closely with theoretical and typical experimental values of 1.0.

F18 determined the temperature sensitivity of creep through the relation between activation energy and stress:

$$\Delta \log \sigma = \frac{1}{n} \left[ \frac{Q}{R} \left( \Delta \frac{1}{T_k} \right) \log(e) - r \Delta \log f_{\text{H}_2\text{O}} \right]. \quad (\text{S15})$$

Using temperature-stepping data from three experimental runs with temperatures ranging between 873 to 1223 K, F18 observed two slopes for low and high temperature regimes. For the high temperature regime (1023 - 1223 K), F18 calculated three values for  $Q$  using previously determined values for  $n$ ,  $f_{\text{H}_2\text{O}}$ , and  $r$ . F18 reported the average value to be  $183 \pm 25 \text{ kJ mol}^{-1}$ , after correcting for changes in water fugacity at different temperatures. F18 explains the change in the temperature sensitivity of creep as due to variability in other flow law parameters such as  $n$  and  $r$ . Although F18 suggest that their estimate of  $Q$  is robust because all the other parameters are also determined at high temperatures, we see that the underlying interactions between parameters are not captured through their linear approach. In Figures S5 and S6, the strain rate-temperature relation determined by F18 is applicable only at high temperatures. Our composite flow law (Figure S5) suggests that the two regimes observed at high and low temperatures may be due to the co-occurrence of dislocation and diffusion creep, which our composite flow law is able to deconvolve.

F18 calculated the grain-size exponent first using data from a deformation experiment in which the annealing period was varied while keeping pressure, temperature, and strain rate constant. Their experiment

assumed that dynamic re-crystallization and grain growth during deformation were minimal. Only one sample was used, which produced five data points. The following relation between stress and grain size was used to determine the grain-size exponent:

$$\Delta \log \sigma = \frac{m}{n} \log d. \quad (\text{S16})$$

From this experiment, F18 determined  $m = 0.43 \pm 0.03$ . F18 also calculated the grain-size exponent using data from four previous experiments in which the starting grain sizes were different. The average grain-size exponent between these two methods was reported as  $m = 0.51 \pm 0.13$ .

Both values of grain-size exponent determined by F18 and by our inversion for GBS are much lower than typical values for grain-size sensitive creep. One possible explanation for this atypical value is that GBS may not be sufficient in describing the deformation regime in which samples are deformed. Our composite inversion shows a distinct shift from diffusion to dislocation creep with increased grain size. When a composite flow law is used to describe F18 data, the diffusion-creep component suggests a grain-size exponent  $m$  of  $2.7 \pm 0.3$ , which is closer to theoretical and typical experimental values. However, as can be seen from Figures S5 and S6, the F18 data look quite noisy in normalized plots, suggesting that the original deformation data are only of modest quality.

## 1.7 Summary

The distributions of flow law parameters for all the inversions are shown in Figure S7, and the mean and standard deviation are given in Table S2.

For the purpose of comparing the rheology between quartz and calcite, we include a calcite flow law determined by Renner, Evans, & Siddiqi (2002). R02 considered a Peierls relation of the form:

$$\dot{\epsilon}_P = A_P \sigma^2 \exp(\sigma/\sigma_P) \exp(-Q_P/RT), \quad (\text{S17})$$

where  $A_P$  is a pre-exponential factor. The resistance to glide is defined as:

$$\sigma_P = (\Sigma_{P,0} + Kd^{-0.5})(T_m - T)$$

where  $\Sigma_{P,0}(T_m - T)$  is the intrinsic Peierls stress and  $Kd^{-m}(T_m - T)$  is the back-stress, described by the grain size  $d$  and the sensitivity to grain size  $m$ .  $T_m$  is the melting temperature for calcite,  $\sim 1600$  K. R02 found this Peierls relation to be most consistently applicable for a range of calcite-bearing rocks. The values providing the best fit were  $\ln A_P \approx 10^{\pm 0.5} \text{ MPa}^{-2} \text{ s}^{-1}$ ,  $\Sigma_{P,0} \approx 7.8 \text{ MPa} \cdot \text{kK}^{-1}$ ,  $K \approx 115 \text{ MPa} \cdot \text{kK}^{-1} \mu\text{m}^{0.5}$ ,  $m = 0.5$ , and  $Q_P \approx 200 \text{ kJ mol}^{-1}$ .

As calcite is known to weaker than quartz in most geological settings, we expect that any strength profile calculated using a quartz flow law must be comparatively stronger than those using the calcite flow law. Given the R02 flow law itself is subject to some uncertainties, it would be reasonable to be suspicious for a flow law that provides a strength profile considerably weaker than that of calcite. With this consideration, our GBS flow law derived from the F18 data (Figure S8, red dot-dashed) may readily be discounted. F18's original GBS flow law predicts quartz strength consistently higher than calcite strength, but this flow law is actually not consistent with their data as indicated by our analysis. Thus, the use of a GBS flow law does not seem to be appropriate when discussing the strength of quartz aggregates.

Regarding strength profiles according to dislocation creep, our flow law based on the RB04ab data provides the strongest profile, whereas our flow law based on the LP92 data results in the weakest one (Figure S8). Our inversion for RB04ab has the highest misfit ( $\chi^2/N$  of 58), and together with its unusually high inter-run biases, the reliability of this flow law (or the original RB04ab data) is rather low. A similar comment applies to our composite-rheology inversion with the F18 data ( $\chi^2/N$  of 10.4). Data misfit is

smallest for the GT95 data ( $\chi^2/N$  of 0.67), and we adopt our flow law based on the GT95 data when calculating the strength of the upper continental crust.

In Figure S8, the prediction based on the flow law proposed by Hirth, Teyssier, & Dunlap (2001) is also shown for comparison (black dashed). The flow law of Hirth et al. (2001) is widely used because it is based on both experimental deformation data and field observations, but their field observations come from a single locality (Ruby Gap duplex, Central Australia), and whereas its deformation history is said to be well constrained, it is still difficult to extract reliable strain rates from a  $\sim 30$ -My-long deformation history. Nevertheless, it is useful as an upper bound on the likely yield stress of quartzite, and it is comforting to see that the predictions from our inversion-based flow laws with GT95 and LP92 data are similar to the prediction of the flow law of Hirth et al. (2001), especially at the temperature of 573 K, which corresponds to their field observations.

To quantify the covariation of parameter uncertainties, we report the correlation coefficients in Tables S3-S7. For each inversion, the correlation coefficient matrix shows the joint variability between each combination of parameters. Correlation coefficients of 1 and -1 refer to perfectly positive and negative correlations, respectively, and a value of 0 refers to no linear correlation. We note that this analysis may reveal linear relationships between parameters, but may not determine whether parameters are independent of each other (i.e. a correlation of zero does not imply that two parameters are independent as they may have a nonlinear relationship.)

In general, we find that dislocation and diffusion creep parameters correlate most to other parameters describing the same deformation mechanism. The correlation between parameters of the same deformation mechanism suggests the importance of simultaneously inverting for all flow-law parameters of a certain deformation mechanism when determining its flow law. Similarly, to a lesser degree, the correlation between parameters of different deformation mechanisms suggests that a simultaneous inversion is also important in the determination of a composite flow law.

## 2 Strain rate modeling

### 2.1 Isostasy

As in the continental freeboard model of Korenaga, Planavsky, & Evans (2017), we adopt the following values for the densities and thicknesses of individual components in our isostasy model:  $\rho_{cc}$  of  $2850 \text{ kg m}^{-3}$ ,  $h_{cm}$  of 200 km,  $\rho_{cm}$  of  $3338 \text{ kg m}^{-3}$  at present and  $3333 \text{ kg m}^{-3}$  at 3 Ga,  $\rho_w$  of  $1000 \text{ kg m}^{-3}$ ,  $h_{oc}$  of 7 km at present and 28.4 km at 3 Ga,  $\rho_{oc}$  of  $2919 \text{ kg m}^{-3}$  at present and  $2957 \text{ kg m}^{-3}$  at 3 Ga,  $h_{om}$  of 53 km at present and 106.5 km at 3 Ga,  $\rho_{om}$  of  $3284 \text{ kg m}^{-3}$  at present and  $3268 \text{ kg m}^{-3}$  at 3 Ga, and  $\rho_m$  of  $3300 \text{ kg m}^{-3}$  at present and  $3271 \text{ kg m}^{-3}$  at 3 Ga. These values are based on the compilation of relevant geological and geophysical observations as well as the theory of mantle melting. The reader is referred to section 3 of Korenaga et al. (2017) for details, but important points may be summarized as follows. The secular evolution of the oceanic domain is based on the cooling history of the upper mantle (Herzberg, Condie, & Korenaga, 2010) and the mantle melting model of Korenaga, Kelemen, & Holbrook (2002). The density of continental crust is based on the compilation of Christensen & Mooney (1995); we assume that it does not change with time, based on the continental growth model of Guo & Korenaga (2020). The thickness of continental lithospheric mantle is inferred from seismic tomography models (Carlson, Pearson, & James, 2005), and the temporal evolution of its density is based on expected changes in thermal and chemical structures (Boyd, 1989; Jordan, 1979; Lee, 2003; Servali & Korenaga, 2018).

## 2.2 Geotherm

To calculate a geotherm, we solve the following one-dimensional heat conduction equation (Jaupart & Mareschal, 2015):

$$k(T)\frac{dT}{dz} = q(z), \quad (\text{S18})$$

where  $k(T)$  is temperature-dependent thermal conductivity and  $q(z)$  is depth-dependent heat flow, with temperature boundary conditions at the surface and at the base of the continental lithospheric mantle. The surface temperature is fixed at 0 °C, and the bottom temperature is set according to mantle potential temperature with an adiabatic gradient of 0.5 K km<sup>-1</sup>. The potential temperature increases with age and peaks at around 3 Ga (Herzberg et al., 2010); we use the potential temperature of 1350 °C for the present and 1350 °C for the Archean (3.5 Ga). Temperature-dependent thermal conductivities for the crust and the mantle are adopted from Whittington, Hofmeister, & Nabelek (2009) and McKenzie, Jackson, & Priestley (2005), respectively. For the present-day concentration of heat producing elements, <sup>238</sup>U, <sup>235</sup>U, <sup>232</sup>Th, and <sup>40</sup>K, we use the bulk crustal composition of Rudnick & Gao (2003), with <sup>238</sup>U/U = 0.9927, <sup>235</sup>U/U = 0.0072, <sup>232</sup>Th/Th = 1, and <sup>40</sup>K/K = 1.28 × 10<sup>4</sup> (Korenaga, 2006). The continental crust is divided into upper, middle, and lower one thirds, with 60%, 34%, and 6% of total crustal heat production, respectively. For heat production within the continental lithospheric mantle, we follow Rudnick, McDonough, & O’Connell (1998). The Archean (3.5 Ga) concentration of heat-producing elements in the continental crust is calculated from their present-day abundances and half-lives for the standard case; we also test the cases of 75% and 50% heat production for comparison.

To quantify the effect of a cold ocean layer on crustal geotherm, we conducted two-dimensional thermal conduction modeling using the finite element code of Korenaga & Jordan (2003) (Figure S9). A reference one-dimensional structure is prepared with depth-dependent internal heat production, which is adjusted to produce a crustal geotherm similar to those considered in this study (Figure 2C). An initial two-dimensional structure is created by setting the temperature of a small rectangular domain at the top-right corner to 0 <sup>circ</sup>C; the temperature of this small domain is kept fixed at 0 <sup>circ</sup>C. As it can be seen from the subsequent evolution Figure S9, a steady state is achieved with a time scale of a few million years, in which only a few kilometers of the continental domain is affected by this introduction of a cold ocean layer.

## 2.3 Strain rate

The flow laws discussed in section 1 is based on deformation experiments conducted in the uniaxial stress setting, whereas the collapse of continental crust by pressure imbalance at the ocean-continental boundary (Figure 1) follows the plane strain setting. These two different settings can be related via equivalent stresses and strain rates (Ranalli, 1995), as follows.

First, we note that a power-law creep may be described with invariants as

$$\dot{\epsilon}_E = C\sigma_E^n, \quad (\text{S19})$$

or in the tensor form

$$\dot{\epsilon}_{ij} = C\sigma_E^{n-1}\sigma_{ij}, \quad (\text{S20})$$

where  $C$  is a constant, and  $\dot{\epsilon}_E$  and  $\sigma_E$  are equivalent strain rate and equivalent deviatoric stress, respectively, defined as  $\sqrt{\dot{\epsilon}_{ij}\dot{\epsilon}_{ij}/2}$  and  $\sqrt{\sigma_{ij}\sigma_{ij}/2}$ .

For the uniaxial stress setting with  $\tau_1$  (which corresponds to differential stress used in a deformation experiment), the principal deviatoric stresses are  $\sigma_1 = 2\tau_1/3$ ,  $\sigma_2 = \sigma_3 = -\tau_1/3$ , and the principal strain rates are described by  $\dot{\epsilon}_2 = \dot{\epsilon}_3 = -\dot{\epsilon}_1/2$ . Thus, the equivalent deviatoric stress is  $\sqrt{3}\tau/3$ , and the equivalent

strain rate is  $\sqrt{3}\dot{\epsilon}_1/2$ . Equation (S19) then indicates

$$\dot{\epsilon}_1 = \frac{2C}{3^{(n+1)/2}}\tau_1^n, \quad (\text{S21})$$

and the factor  $2C/3^{(n+1)/2}$  corresponds to the pre-exponential factor of an experimental flow law.

For the plane strain setting, if we take the direction parallel to the ocean-continent boundary as the first coordinate, the principal strain rates are described by  $\dot{\epsilon}_1 = 0$  and  $\dot{\epsilon}_2 = -\dot{\epsilon}_3$ . The principal stresses are lithostatic pressure in the continental domain for the first and third (vertical) coordinates and the difference between lithostatic pressures at the ocean-continent boundary for the second coordinate (perpendicular to the boundary). If we denote the pressure difference by  $\Delta\tau$ , the principal deviatoric stresses are  $\sigma_1 = \sigma_3 = \Delta\tau/3$  and  $\sigma_2 = -2\Delta\tau/3$ . Thus, the equivalent strain rate is simply  $\dot{\epsilon}_2$ , and the equivalent deviatoric stress is  $\sqrt{3}\Delta\tau/3$ . Thus,

$$\dot{\epsilon}_2 = \frac{C}{3^{n/2}}\Delta\tau^n \quad (\text{S22})$$

$$= \frac{\sqrt{3}}{2}A\Delta\tau^n, \quad (\text{S23})$$

where  $A$  is the pre-exponential factor of an experimental flow law. Thus, a strain rate prediction from an experimental flow law needs to be multiplied by a factor of  $\sqrt{3}/2$ .

## References

- Aines, R. D., Kirby, S. H., & Rossman, G. R. (1984). Hydrogen speciation in synthetic quartz. *Phys. Chem. Minerals*, *11*, 204-212, doi:10.1007/bf00308135.
- Boyd, F. R. (1989). Compositional distinction between oceanic and cratonic lithosphere. *Earth Planet. Sci. Lett.*, *96*, 15-26.
- Carlson, R. W., Pearson, D. G., & James, D. E. (2005). Physical, chemical, and chronological characteristics of continental mantle. *Rev. Geophys.*, *43*, RG1001, doi:10.1029/2004RG000156.
- Christensen, N. I., & Mooney, W. D. (1995). Seismic velocity structure and composition of the continental crust: A global view. *J. Geophys. Res.*, *100*, 9761-9788.
- Fukuda, J., Holyoke, C. W., & Kronenberg, A. K. (2018). Deformation of fine-grained quartz aggregates by mixed diffusion and dislocation creep. *Journal of Geophysical Research: Solid Earth*, *123*, 4676-4696, <https://doi.org/10.1029/2017jb015133>.
- Gleason, G. C., & Tullis, J. (1993). Improving flow laws and piezometers for quartz and feldspar aggregates. *Geophys. Res. Lett.*, *20*, 2111-2114. doi: 10.1029/93gl02236
- Gleason, G. C., & Tullis, J. (1995). A flow law for dislocation creep of quartz aggregates determined with the molten salt cell. *Tectonophysics*, *247*, 1-23.
- Guo, M., & Korenaga, J. (2020). Argon constraints on the early growth of felsic continental crust. *Sci. Adv.*, *6*, eaaz6234.
- Herzberg, C., Condie, K., & Korenaga, J. (2010). Thermal evolution of the Earth and its petrological expression. *Earth Planet. Sci. Lett.*, *292*, 79-88.
- Hirth, G., Teyssier, C., & Dunlap, W. J. (2001). An evaluation of quartzite flow laws based on comparisons between experimentally and naturally deformed rocks. *Int. J. Earth Sciences*, *90*, 77-87.
- Holyoke, C. W., & Kronenberg, A. K. (2010). Accurate differential stress measurement using the molten salt cell and solid salt assemblies in the Griggs apparatus with applications to strength, piezometers and rheology. *Tectonophysics*, *494*, 17-31.
- Jaupart, C., & Mareschal, J.-C. (2015). Heat flow and thermal structure of the lithosphere. In *Treatise on Geophysics*, 2nd ed. (Vol. 6, p. 217-253). Elsevier.

- Jordan, T. H. (1979). Mineralogies, densities and seismic velocities of garnet lherzolites and their geophysical implications. In *The mantle sample: Inclusions in kimberlites and other volcanics* (p. 1-14). AGU.
- Karato, S. (2008). *Deformation of earth materials: Introduction to the rheology of the solid earth*. New York: Cambridge.
- Korenaga, J. (2006). Archean geodynamics and the thermal evolution of Earth. In K. Benn, J.-C. Mareschal, & K. Condie (Eds.), *Archean geodynamics and environments* (p. 7-32). Washington, D.C.: American Geophysical Union.
- Korenaga, J., & Jordan, T. H. (2003). Physics of multiscale convection in Earth's mantle: Onset of sub-lithospheric convection. *J. Geophys. Res.*, *108*(B7), 2333, doi:10.1029/2002JB001760.
- Korenaga, J., & Karato, S. (2008). A new analysis of experimental data on olivine rheology. *J. Geophys. Res.*, *113*, B02403, doi:10.1029/2007JB005100.
- Korenaga, J., Kelemen, P. B., & Holbrook, W. S. (2002). Methods for resolving the origin of large igneous provinces from crustal seismology. *J. Geophys. Res.*, *107*(B9), 2178, doi:10.1029/2001JB001030.
- Korenaga, J., Planavsky, N. J., & Evans, D. A. D. (2017). Global water cycle and the coevolution of Earth's interior and surface environment. *Phil. Trans. R. Soc. A*, *375*, 20150393, doi:10.1098/rsta.2015.0393.
- Kronenberg, A. K., & Tullis, J. (1984). Flow strengths of quartz aggregates: grain size and pressure effects due to hydrolytic weakening. *J. Geophys. Res.*, *89*, 4281-4297.
- Lee, C.-T. A. (2003). Compositional variation of density and seismic velocities in natural peridotites at STP conditions: implications for seismic imaging of compositional heterogeneities in the upper mantle. *J. Geophys. Res.*, *108*, 2441, doi:10.1029/2003JB002413.
- Lu, L. X., & Jiang, D. (2019). Quartz flow law revisited: the significance of pressure dependence of the activation enthalpy. *J. Geophys. Res. Solid Earth*, *124*, 241-256, <https://doi.org/10.1029/2018jb016226>.
- Luan, F. C., & Paterson, M. S. (1992). Preparation and deformation of synthetic aggregates of quartz. *J. Geophys. Res.*, *97*, 301-320.
- McKenzie, D., Jackson, J., & Priestley, K. (2005). Thermal structure of oceanic and continental lithosphere. *Earth Planet. Sci. Lett.*, *233*, 337-349.
- Mullet, B. G., Korenaga, J., & Karato, S.-I. (2015). Markov chain Monte Carlo inversion for the rheology of olivine single crystals. *J. Geophys. Res. Solid Earth*, *120*, 3142-3172, doi:10.1002/2014JB011845.
- Pitzer, K. S., & Sterner, S. M. (1994). Equations of state valid continuously from zero to extreme pressures for h<sub>2</sub>o and co<sub>2</sub>. *J. Chem. Phys.*, *101*, 3111-3116, <https://doi.org/10.1063/1.467624>.
- Ranalli, G. (1995). *Rheology of the earth, 2nd ed.* Springer.
- Renner, J., Evans, B., & Siddiqi, G. (2002). Dislocation creep of calcite. *J. Geophys. Res.*, *107*(B12), 2364, doi:10.1029/2001JB001680.
- Rudnick, R. L., & Gao, S. (2003). Composition of the continental crust. In H. D. Holland & K. K. Turekian (Eds.), *Treatise on Geochemistry* (Vol. 3, p. 1-64). Elsevier.
- Rudnick, R. L., McDonough, W. F., & O'Connell, R. J. (1998). Thermal structure, thickness and composition of continental lithosphere. *Chem. Geol.*, *145*, 395-411.
- Rutter, E. H., & Brodie, K. H. (2004a). Experimental grain size-sensitive flow of hot-pressed Brazilian quartz crystals. *J. Struct. Geol.*, *26*, 2011-2023.
- Rutter, E. H., & Brodie, K. H. (2004b). Experimental intracrystalline plastic flow in hot-pressed synthetic quartzite prepared from Brazilian quartz crystals. *J. Struct. Geol.*, *26*, 259-270.
- Servali, A., & Korenaga, J. (2018). Oceanic origin of continental mantle lithosphere. *Geology*, *46*, 1047-1059.
- Sterner, S. M., & Pitzer, K. S. (1994). An equation of state for carbon dioxide valid from zero to extreme pressures. *Contrib. Mineral. Petrol.*, *117*, 362-374, <https://doi.org/10.1007/bf00307271>.
- Tullis, J., & Yund, R. A. (1982). Grain growth kinetics of quartz and calcite aggregates. *J. Geol.*, *90*, 301-318.

Whittington, A. G., Hofmeister, A. M., & Nabelek, P. I. (2009). Temperature-dependent thermal diffusivity of the Earth's crust and implications for magmatism. *Nature*, 458, 319-321.

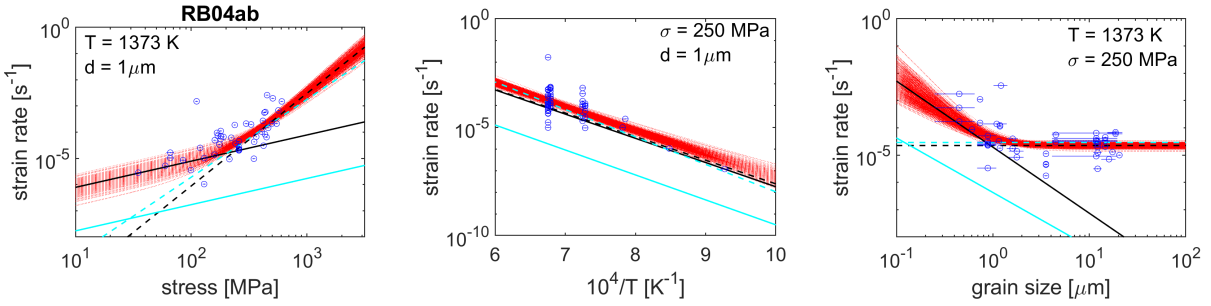


Figure S1: Mean predictions from dislocation (dotted) and diffusion (solid) flow laws from composite inversion (black) on RB04ab data, compared to predictions based on the original flow law of RB04a and RB04b (blue). Strain rate vs. stress, temperature, and grain size relationships are shown from left to right. Normalized data are shown in open circles, and the predictions of  $\sim 10^3$  flow laws are shown in red.

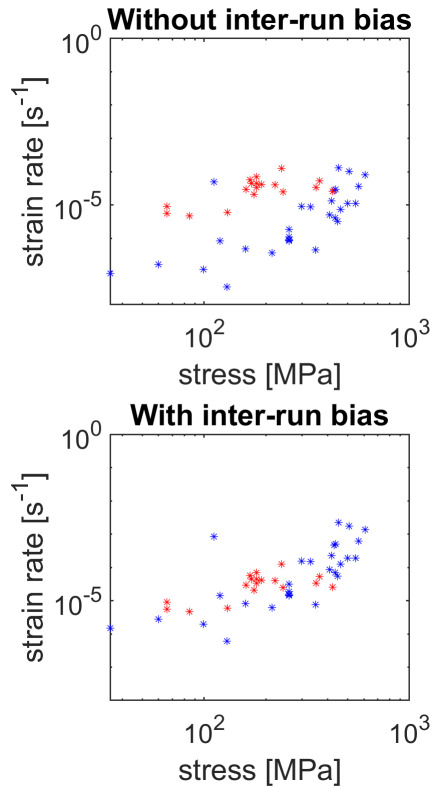


Figure S2: Comparison of RB04a (red) and RB04b (blue) data before and after correcting for inter-run bias, which has a mean of  $10^{-2.8}$ .

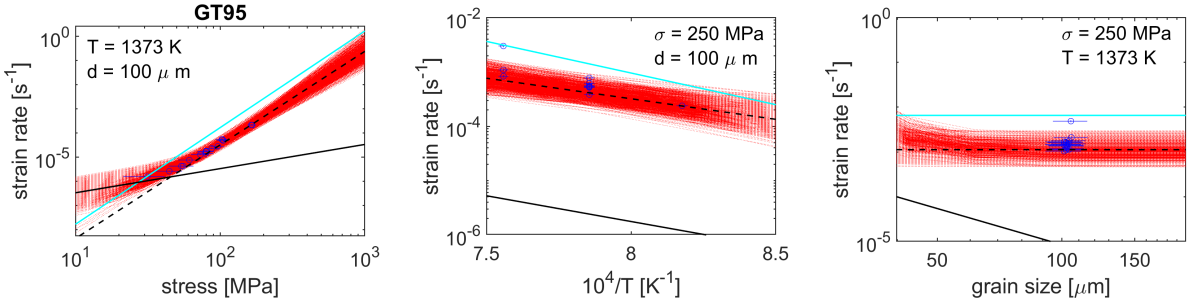


Figure S3: Same as Figure S1, but with GT95 data.

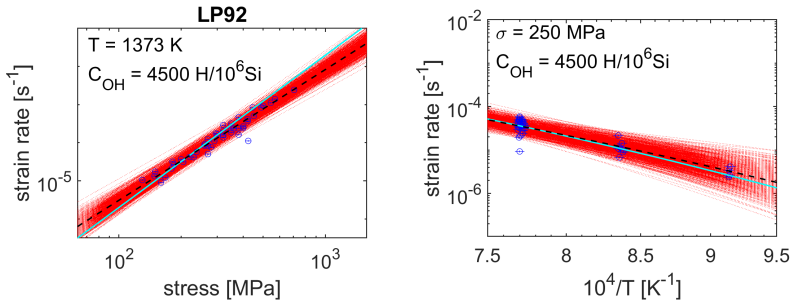


Figure S4: Same as Figure S1, but with LP92 data.

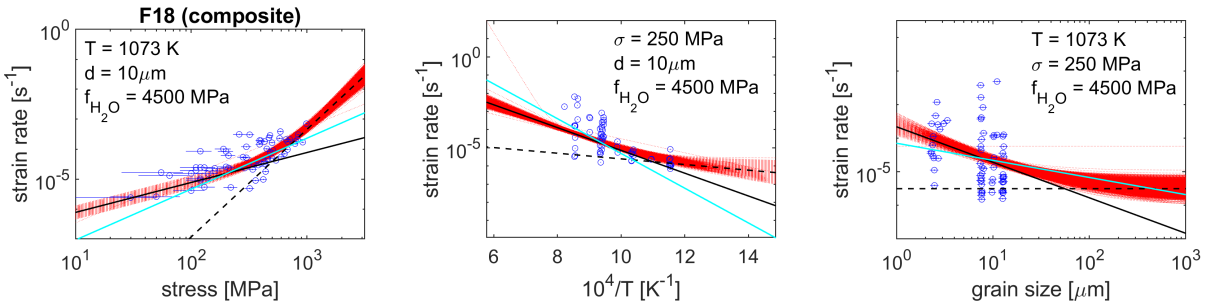


Figure S5: Same as Figure S1, but with F18 data.

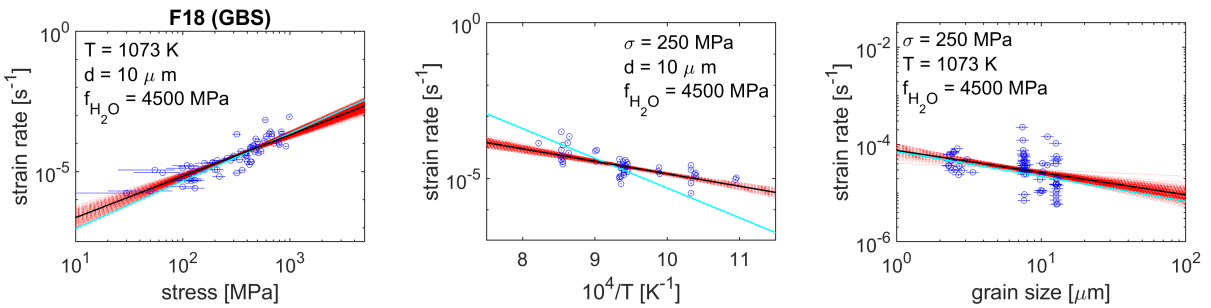


Figure S6: Mean predictions from our inverted GBS flow law based on F18 data (black), compared to predictions from the original F18 GBS flow law (blue).

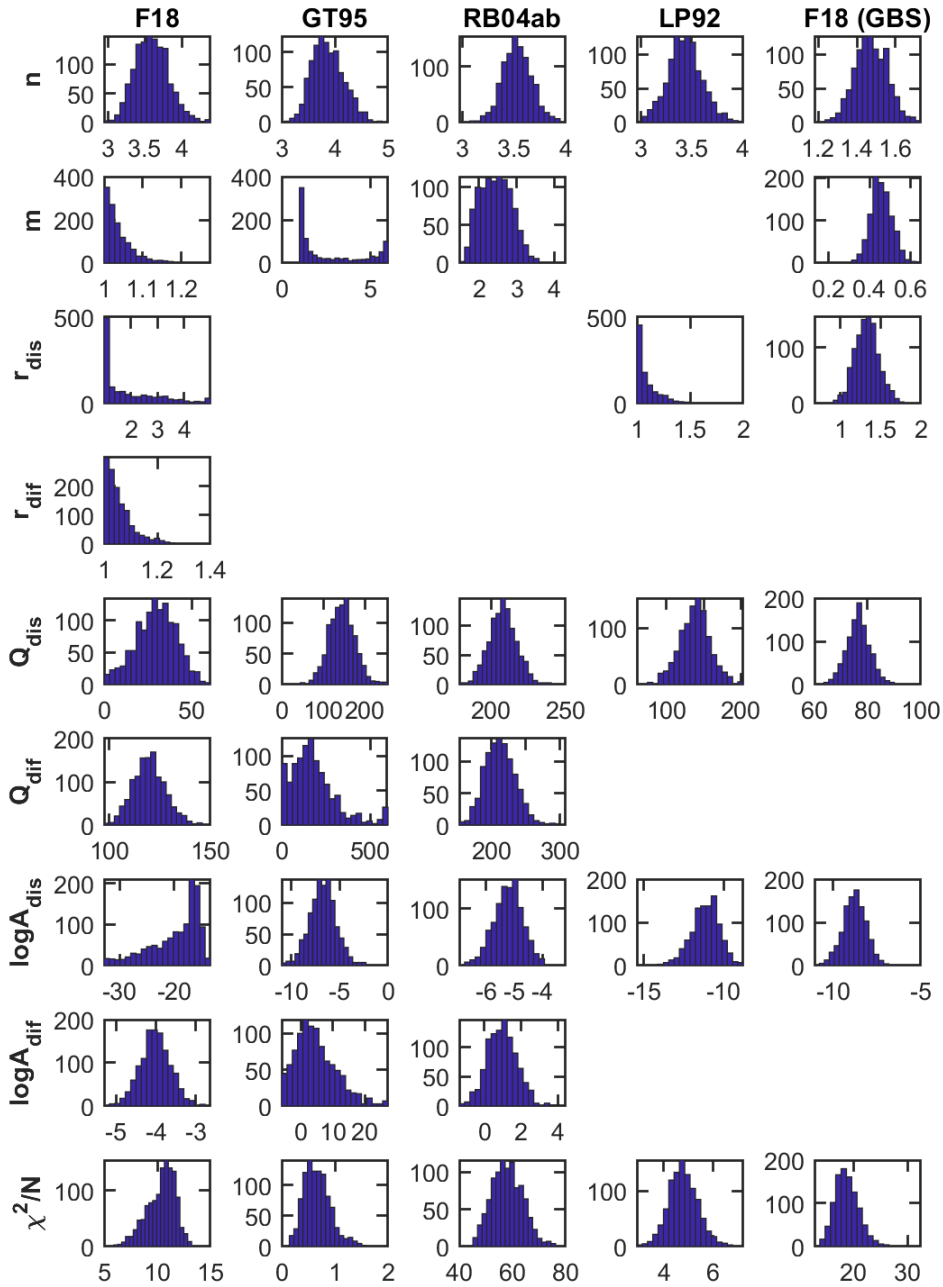


Figure S7: Summary of MCMC inversions for each deformation data set.

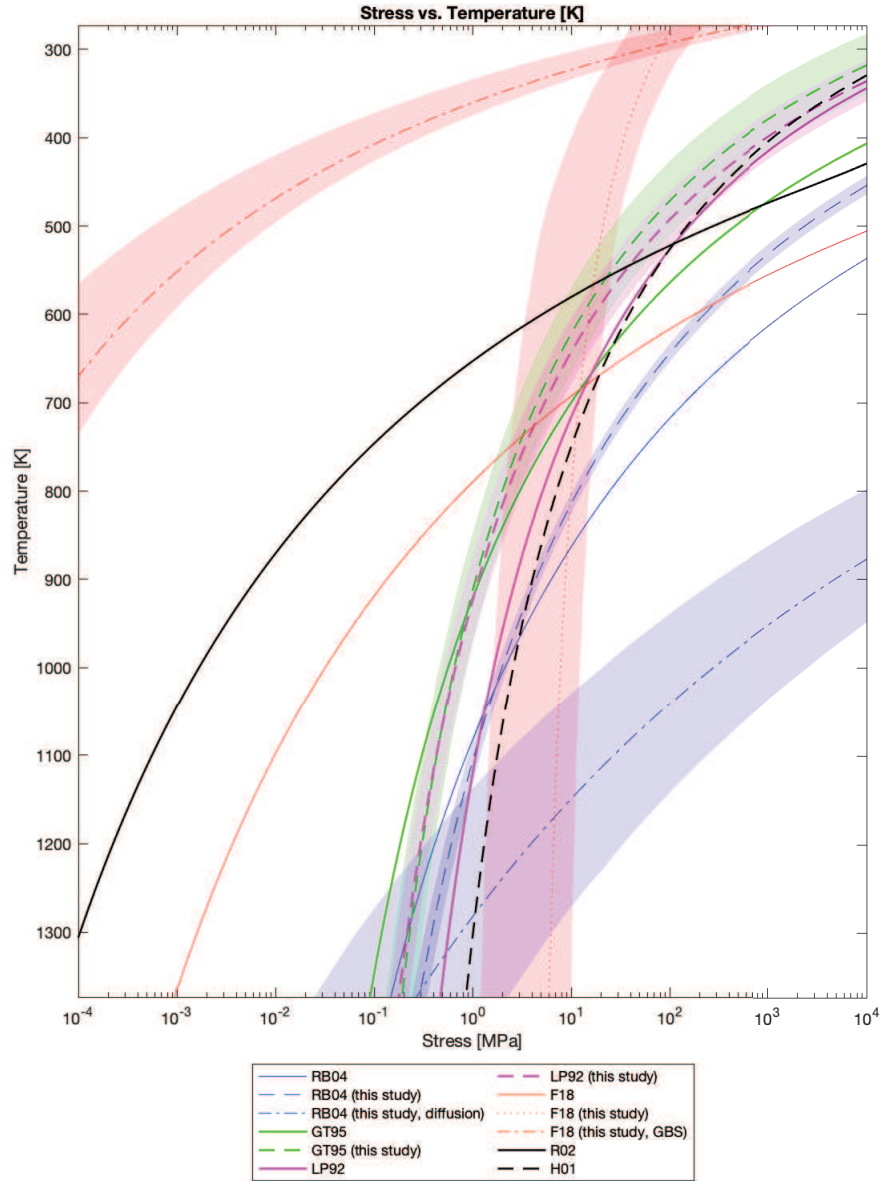


Figure S8: Comparison between strength profiles based on original flow laws and our inverted flow laws. Strain rate of  $10^{-15} \text{ s}^{-1}$  is assumed. Dislocation creep was used to calculate the strength profiles in this study, unless otherwise specified. For grain-size sensitive creep, a grain size of 1 mm is assumed.

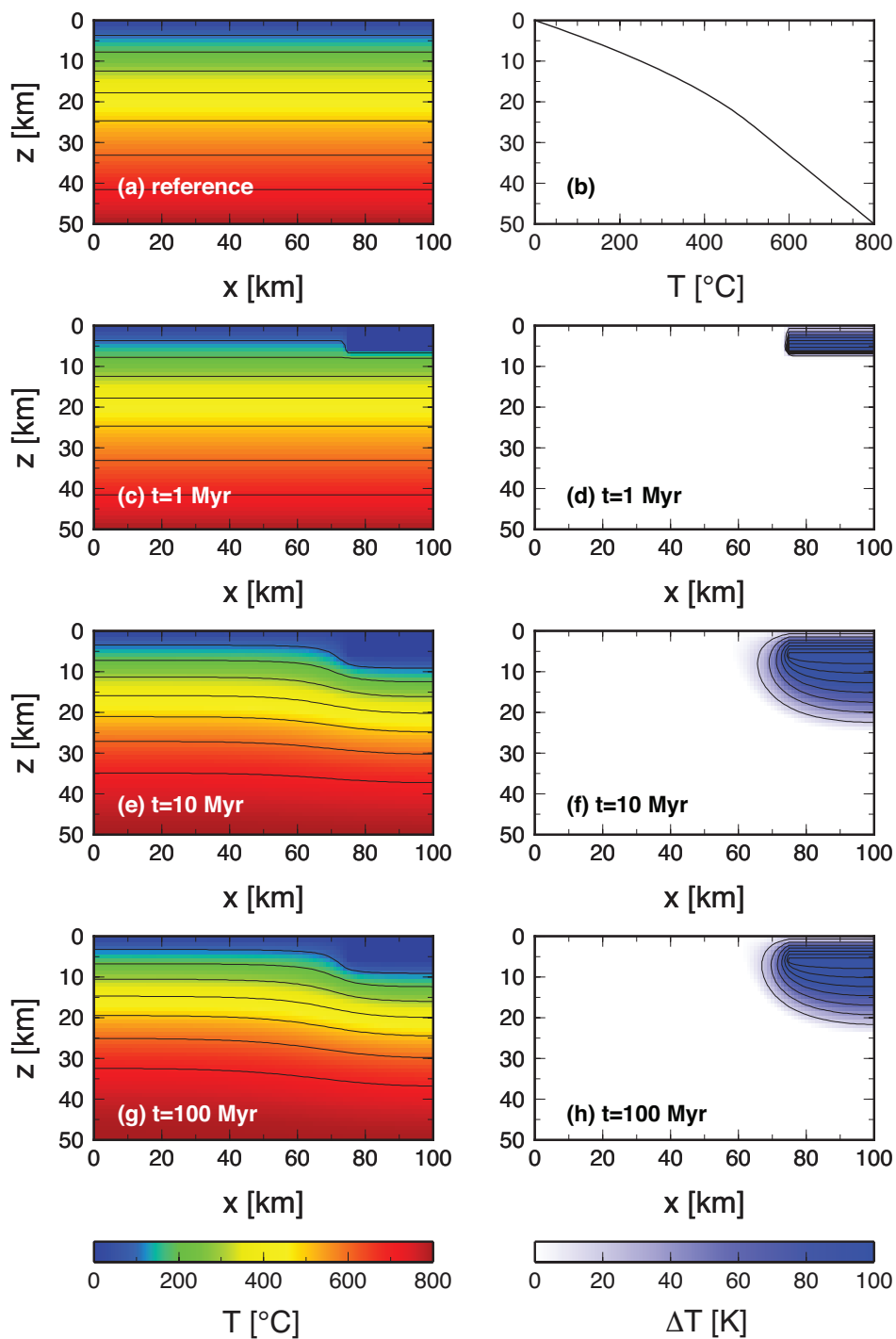


Figure S9: Thermal conduction modeling to quantify the influence of an ocean layer on crustal geotherm. (a) and (b) 1-D reference model, before the introduction of a cold ocean layer. (c) 1 Myr, (e) 10 Myr, and (g) 100 Myr after the introduction of a 6.25-km-high and 25-km-wide cold domain at the top-right corner. (d)-(h) show corresponding temperature differences with respect to the 1-D reference model.

Reference	$\log_{10} A$ [ $\text{MPa}^{-m-n} \text{s}^{-1}$ ]	$n$	$m$	$r$	$Q$ [ $\text{kJ mol}^{-1}$ ]
RB04a	$-4.93 \pm 0.34$	$2.97 \pm 0.29$	–	1.0	$242 \pm 24$
RB04b	$-0.4 \pm 2.1$	$1.0 \pm 0.14$	$2.0 \pm 0.75$	–	$220 \pm 55$
GT95 (without melt)	$-3.96 \pm 2.0$	$4.0 \pm 0.9$	–	1.0	$223 \pm 56$
	$-3.29^{\text{a}}$				
LP92 (silicic acid origin)	$-7.92^{\text{b}}$	$4.0 \pm 0.8$	–	–	$152 \pm 71$
F18	$-2.97 \pm 0.23$	$1.7 \pm 0.2$	$0.51 \pm 0.13$	$1.0 \pm 0.2$	$183 \pm 25$

<sup>a</sup> Re-calculated following the flow stress calibration of Holyoke and Kronenberg (2010).

<sup>b</sup> Calculated in Lu and Jiang (2019).

Table S1: Summary of flow laws suggested by the experimental studies considered in this study.

	$\log_{10} A_{\text{dis}}$	$\log_{10} A_{\text{dif}}$	$n$	$m$	$r_{\text{dis}}$	$r_{\text{dif}}$	$Q_{\text{dis}}$	$Q_{\text{dif}}$
RB04ab	$-5.2 \pm 1.0$	$1.0 \pm 1.6$	$2.4 \pm 0.8$	$3.5 \pm 0.3$	–	–	$208 \pm 19$	$213 \pm 42$
GT95	$-6.7 \pm 1.4$	$4.8 \pm 6.3$	$3.9 \pm 0.3$	$2.7 \pm 1.8$	–	–	$145 \pm 31$	$182 \pm 129$
LP92	$-11.2 \pm 1.8$	–	$3.4 \pm 0.3$	–	$1.1 \pm 0.3$	–	$138 \pm 42$	–
F18	$-19.7 \pm 4.4$	$-4.0 \pm 0.4$	$3.6 \pm 0.2$	$1.06 \pm 0.05$	$1.9 \pm 1.1$	$1.04 \pm 0.08$	$30 \pm 12$	$120 \pm 12$
F18 (GBS)	$-8.8 \pm 0.7$	–	$1.48 \pm 0.08$	$0.46 \pm 0.05$	$1.3 \pm 0.15$	–	$76 \pm 5$	–

Table S2: Mean and standard deviations for inversion parameters.

	$\log_{10} A_{\text{dis}}$	$\log_{10} A_{\text{dif}}$	$n$	$m$	$Q_{\text{dis}}$	$Q_{\text{dif}}$
$\log_{10} A_{\text{dis}}$	1.000	-0.174	-0.748	0.514	0.795	-0.118
$\log_{10} A_{\text{dif}}$	-0.174	1.000	0.054	0.176	-0.219	0.973
$n$	-0.748	0.054	1.000	-0.386	-0.204	-0.026
$m$	0.514	0.176	-0.386	1.000	0.369	0.227
$Q_{\text{dis}}$	0.795	-0.219	-0.204	0.369	1.000	-0.224
$Q_{\text{dif}}$	-0.118	0.973	-0.026	0.227	-0.224	1.000

Table S3: Correlation coefficients between all inversion parameters for RB04ab.

	$\log_{10} A_{\text{dis}}$	$\log_{10} A_{\text{dif}}$	$n$	$m$	$Q_{\text{dis}}$	$Q_{\text{dif}}$
$\log_{10} A_{\text{dis}}$	1.000	0.007	-0.378	0.012	0.892	0.020
$\log_{10} A_{\text{dif}}$	0.007	1.000	-0.131	0.614	-0.070	0.816
$n$	-0.378	-0.131	1.0000	-0.0732	0.0782	-0.1344
$m$	0.012	0.614	-0.073	1.000	-0.024	0.050
$Q_{\text{dis}}$	0.892	-0.070	0.078	-0.024	1.000	-0.061
$Q_{\text{dif}}$	0.020	0.816	-0.134	0.050	-0.061	1.000

Table S4: Correlation coefficients between all inversion parameters for GT95.

	$\log_{10} A$	$n$	$r$	$Q$
$\log_{10} A$	1.000	-0.157	-0.482	0.730
$n$	-0.157	1.000	0.0407	0.3667
$r$	-0.482	0.04	1.000	0.040
$Q$	0.730	0.367	0.040	1.000

Table S5: Correlation coefficients between all inversion parameters for LP92.

	$\log_{10} A_{\text{dis}}$	$\log_{10} A_{\text{dif}}$	$n$	$m$	$r_{\text{dis}}$	$r_{\text{dif}}$	$Q_{\text{dis}}$	$Q_{\text{dif}}$
$\log_{10} A_{\text{dis}}$	1.000	0.140	-0.273	-0.041	-0.970	0.052	0.677	0.155
$\log_{10} A_{\text{dif}}$	0.140	1.000	-0.383	0.008	-0.050	0.004	0.283	0.764
$n$	-0.273	-0.383	1.000	0.053	0.049	-0.160	-0.584	-0.430
$m$	-0.041	0.008	0.053	1.000	0.022	0.020	-0.100	-0.081
$r_{\text{dis}}$	-0.970	-0.050	0.049	0.022	1.000	-0.020	-0.506	-0.055
$r_{\text{dif}}$	0.052	0.004	-0.160	0.020	-0.020	1.000	0.073	0.633
$Q_{\text{dis}}$	0.677	0.283	-0.584	-0.100	-0.506	0.073	1.000	0.310
$Q_{\text{dif}}$	0.155	0.764	-0.430	-0.081	-0.055	0.633	0.310	1.000

Table S6: Correlation coefficients between all inversion parameters for F18.

	$\log_{10} A$	$n$	$m$	$r$	$Q$
$\log_{10} A$	1.000	-0.225	-0.277	-0.945	0.544
$n$	-0.225	1.000	0.174	0.059	0.362
$m$	-0.277	0.174	1.000	0.302	-0.136
$r$	-0.945	0.060	0.302	1.000	-0.404
$Q$	0.544	0.362	-0.136	-0.404	1.000

Table S7: Correlation coefficients between all inversion parameters for F18 (GBS).